Geothermal Heating in the Panama Basin. Part II: Abyssal Water Mass Transformation

D. Banyte[1], **M. Morales Maqueda[1]**, **D. A. Smeed[2]**, **A. Megann[2]**, **R. Hobbs[3]**, and **S. Recalde[4]**

[1]School of Marine Science and Technology, University of Newcastle upon Tyne, Newcastle upon Tyne, UK, [2]National Oceanography Centre, Southampton, UK, [3]Department of Earth Sciences, University of Durham, Durham, UK, [4]Instituto Oceanográfico de la Armada, Guayaquil, Ecuador

Abstract Diabatic upwelling of abyssal waters is investigated in the Panama Basin employing the water mass transformation framework of Walin (1982). We find that, in large areas of the basin, the bottom boundary layer is very weakly stratified and extends hundreds of meters above the sea floor. Within the weakly stratified bottom boundary layer, neutral density layers intercept the bottom of the basin. The area of these density layer incrops increases gradually as the abyssal waters become lighter. Large incrop areas are associated with strong diabatic upwelling of abyssal water, geothermal heating being the largest buoyancy source. While a significant amount of water mass transformation is due to extreme turbulence downstream of the Ecuador Trench, the only abyssal water inflow passage, water mass transformation across the upper boundary of abyssal water layer is accomplished almost entirely by geothermal heating.

Plain Language Summary This study investigates how abyssal waters become lighter with the focus on geothermal heating effect. We find that in the Panama Basin, geothermal heating dominates the upwelling across the upper boundary of abyssal waters. Nevertheless, high turbulence at the abyssal water inflow passage contributes significantly to lighten the densest waters. Finally, most of the upwelling is found in the weakly stratified bottom boundary layer, which is hundreds of meters thick, contrary to the common assumption of it being just meters to 10s of meters thick.

1. Introduction

The diabatic upwelling of abyssal waters is arguably the least well understood part of the meridional overturning circulation. Introduced by Stommel (1958), the picture of homogeneous, widespread upwelling driven by turbulent mixing with an average diffusivity of 10^{-4} m²/s (Munk, 1966) was challenged by direct measurements of deep turbulent dissipation (Polzin et al., 1997). Deep ocean turbulence turns out to be highly inhomogeneous: at least an order of magnitude larger than the canonical estimate of Munk (1966) in narrow passages and canyons, and over rough bathymetry, but an order of magnitude smaller in most of the rest of the ocean. Consequently, there is a prevailing notion that the bulk of the abyssal water upwelling occurs in localized regions of complex and rough bathymetry.

In recent years, however, it has been argued that bottom-intensified mixing could lead to deep waters becoming denser, rather than lighter, and therefore to diabatic downwelling, rather than upwelling (de Lavergne et al., 2016; Ferrari et al., 2016; Klocker & McDougall, 2010). The density flux due to diapycnal mixing is commonly parametrized as $K^z \gamma_z$, where K^z is the vertical turbulent diffusivity and γ_z is the vertical density gradient. In the deep ocean, stratification rapidly increases upward. Thus, if turbulent diffusivity was uniform in the vertical, the stronger density flux at lighter densities would cause density flux divergence, that is, buoyancy convergence, or diabatic upwelling. However, observations show that turbulent kinetic energy dissipation can rapidly increase with depth above rough bathymetry (e.g., Ledwell et al., 2000). Assuming that the turbulent density flux varies similarly to turbulent kinetic energy in the vertical, this could lead to a density flux convergence and, consequently, to diabatic downwelling. A conundrum arises in the observation that vast areas of the deep ocean have favorable conditions for diabatic upwelling to occur, but turbulent mixing is too weak there (small K^z) to generate as much diabatic upwelling of abyssal waters as we know is needed to support the global meridional overturning circulation. At the same time, regions of vigorous, bottom-intensified turbulent mixing imply diabatic downwelling, instead of upwelling.
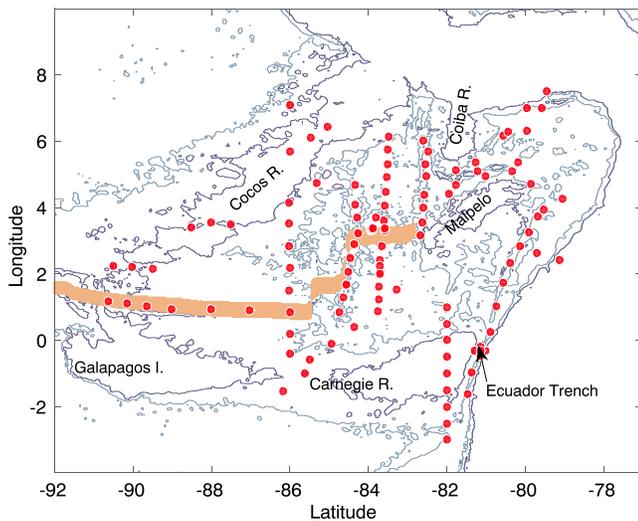
Figure 1. The bathymetry of the Panama Basin. Red dots indicate the locations of conductivity-temperature-depth casts collected between December 2014 and March 2015. Bathymetry contours mark the depths of 2,000 and 3,000 m. The thick, brown line marks the location of geothermal heating larger than 500 mW/m^2.

Several solutions have been suggested to solve this puzzle. Klocker and McDougall (2010) observed that, since the area of ocean basins decreases with depth, the net (integrated) density flow across a given isopycnal of area S_0 can still be larger than the flux across a deeper isopycnal of area S_1, even if K_z increases with depth, resulting in density flux divergence over the bounded density layer or diabatic upwelling. Following Jackett and McDougall (1997), we define an isopycnal as a surface of neutral density γ, where we subtract 1,000 kg/m^3 from the neutral density values. The difference between the two density surface areas, $S_0 - S_1$, is called the density layer intercept with the bottom of the basin. It has been hypothesized that abyssal water upwelling happens along the bottom boundaries of the basin and is predominantly set by the size of the bottom intercept areas of the density layers (de Lavergne et al., 2016; Ferrari et al., 2016; McDougall & Ferrari, 2017).

Geothermal heating, acting solely at the bottom boundary, contributes to buoyancy flux convergence within the weakly stratified bottom boundary layer (wsBBL). Modeling studies of various levels of complexity (e.g., Adcroft et al., 2001; Emile-Geay & Madec, 2009; Hofmann & Morales Maqueda, 2009) have debated the importance of geothermal heating for water mass transformation with simulated contributions ranging from negligible to over 30%. Using climatologies of hydrographic properties and available energy fluxes from baroclinic tides and lee waves combined with the near-field mixing parametrization, de Lavergne et al. (2016) find a 40% contribution of geothermal heating to the upwelling of the Antarctic Bottom Waters.

The purpose of this study is to compare new observational evidence with the developing theories on abyssal water mass transformation. We investigate the semienclosed Panama Basin using recently collected high-resolution hydrographic data. We adopt the water mass transformation framework of Walin (1982), as explained in section 3, to evaluate the importance of geothermal heating for abyssal water diapycnal upwelling (section 4).

2. The Panama Basin

The Panama Basin is almost completely shielded from the rest of the equatorial Pacific Ocean below about 2,500 m (Figure 1). The only deep water exchange pathway is a passage between the Carnegie Ridge and the South American continental slope called the Ecuador Trench, with a sill depth of about 2,930 m. An inflow through the trench into the basin at a rate of 0.29 ± 0.07 Sv with neutral density range between 28.016 and 27.967 kg/m^3 was estimated in the first part of this study (Banyte, Smeed, et al., 2018). In this study, we show that the discretized density layer $\gamma = 27.970 \pm 0.001$ kg/m^3 has the largest incrop area and consequently the largest water mass transformation rate in the wsBBL driven by the geothermal heating. We conclude that the upper boundary of the abyssal water layer is between density surfaces $\gamma_{27.967}$ and $\gamma_{27.970}$. For simplicity, in this study the density surface $\gamma_{27.970}$ is named the upper boundary of the abyssal water layer.

Hydrography reveals that abyssal waters entering the basin experience a strong transformation in the first 200 km downstream of the inflow (Banyte, Smeed, et al., 2018). Over this short distance, all waters denser than 27.988 kg/m^3 are transformed into lighter waters. The observed bottom density change of 0.028 kg/m^3 is also reflected in a bottom temperature rise of 0.15 °C. Banyte, Smeed, et al. (2018) hypothesized that the intense turbulent mixing leading to this dramatic water mass transformation is caused by a hydraulic jump resulting from critical flow through the passage. Abyssal water mass transformation further into the basin is much more gradual and the bottom density change is estimated to be 0.021 kg/m^3 (0.10 °C).

3. Theory: Abyssal Water Transformation

Abyssal water mass transformation inside the basin is analyzed using the water mass transformation framework of Walin (1982), assuming steady state conditions for a volume of fluid, ΔV, bound by neutral density surfaces, γ and $\gamma + \Delta\gamma$. In general, we follow the notation of Nurser et al. (1999) and use their derivation of volume and mass conservation for the volume of fluid. The lateral flux of fluid into ΔV is denoted by $\Delta\Psi$, the
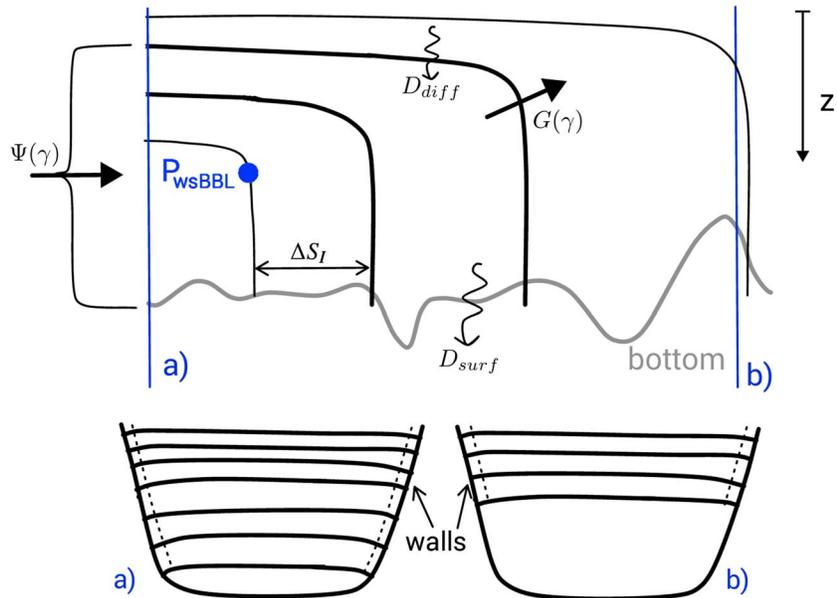
Figure 2. Schematics of discretized density layers in an idealized basin along meridional transect (top) and two zonal transects: near to the source (a) and further into the basin (b). The net inflow into the basin between the seabed and the isopycnal layer γ is denoted by $\Psi(\gamma)$. Similarly, $G(\gamma)$ denotes the net water mass transformation rate across the density surface γ. Diffusive and geothermal density fluxes are marked by D_{diff} and D_{surf}. The top figure visualizes formation of incrops with the area of ΔS_I, while zonal transects below—formation of bottom intercept areas at the sloping walls of the basin. wsBBL = weakly stratified bottom boundary layer.

diabatic flows (water mass transformation) through the bounding density surfaces are denoted by $G(\gamma)$ and $G(\gamma + \Delta\gamma)$ (Figure 2). The analysis makes the approximation that all density transformations are due to either geothermal heat fluxes or turbulent mixing, neglecting the effects of cabbeling, thermobaricity, and neutral helicity. Unlike Nurser et al. (1999), however, we choose $G(\gamma)$ to be positive in the direction of decreasing density (or decreasing depth). Thus, by this definition, water mass transformation leading to lighter water is positive ($G(\gamma) > 0$):

$$G(\gamma) = \frac{\partial D_{diff}(\gamma)}{\partial \gamma} + \frac{\partial D_{surf}(\gamma)}{\partial \gamma},$$ (1)

where D_{diff} is the net turbulent density flux across isopycnal γ, positive in the direction of increasing densities, and D_{surf} is the surface density outflux through the seabed of all the water denser than γ and is caused by geothermal heating.

Equation (1) links the rate of water mass transformation to the processes causing the said transformation. A diapycnal volume flux directed from dense to light water $G(\gamma) > 0$ requires a divergence of density fluxes driven either by turbulence, $\partial D_{diff}/\partial \gamma > 0$, or by geothermal heating, $\partial D_{surf}/\partial \gamma > 0$.

The integrated downgradient diffusive density flux across the isopycnal γ of area $S_D(\gamma)$ can be expressed as

$$D_{diff}(\gamma) = - < F(\gamma) > S_D(\gamma),$$ (2)

where $F(\gamma)$ is upgradient density flux that is sometimes parametrized through diapycnal vertical diffusivity K^z and density gradient γ_z as $F(\gamma) = -K^z \gamma_z$, with z increasing downward. The density fluxes in equation (2) are averaged over the whole isopycnal as

$$< F(\gamma) > = \frac{1}{S_D(\gamma)} \int_{S_D(\gamma)} F dS_D.$$ (3)

Similarly, $D_{surf}(\gamma)$ can be expressed as

$$D_{surf}(\gamma) = -\frac{\alpha}{C_p} < q(\gamma) > S_F(\gamma),$$ (4)

where α is the thermal expansion coefficient of seawater and C_p is the heat capacity of seawater. Both are considered to be constant. $< q(\gamma) >$ is the average geothermal heat flux over the sea floor region of area $S_F(\gamma)$ located underneath isopycnal γ:

$$< q(\gamma) > = \frac{1}{S_F(\gamma)} \int_{S_F(\gamma)} q \, dS_F, \tag{5}$$

where q is the in situ geothermal heat flux.

Introducing equations (2) and (4) in equation (1), we reach the following expression.

$$G(\gamma) = g_{dF} + g_{dq} + g_F + g_q =$$
$$= -\left(\frac{\partial F(\gamma)}{\partial \gamma} + \frac{\alpha}{C_p} \frac{\partial q}{\partial \gamma} \right) S - \left(F(\gamma) + \frac{\alpha}{C_p} q \right) \frac{\partial S}{\partial \gamma}, \tag{6}$$

where, for convenience, we have dropped the angle brackets from the average quantities defined in equations (3) and (5). We have also made the approximation $S_D \simeq S_F = S$.

The $\partial S / \partial \gamma$ is always negative, because horizontal area of isopycnals is increasing with lighter densities located higher up in the water column. The increase in S happens due to the access of lighter waters to the boundary, either the bottom of the basin or its walls (Figure 2). Hence, $(\partial S / \partial \gamma) \Delta \gamma$ denotes the bottom intercept area, which is a sum of incrop area at the bottom of the basin and bottom intercepts at the basin walls.

As $\partial S / \partial \gamma$ is negative, the terms g_F and g_q in equation 6 are always positive. The term g_{dq}, which represents spatial variation of geothermal heating, we show, is also positive in the Panama Basin. The only negative term in equation 6 is expected to be g_{dF} on the condition that density fluxes F are bottom intensified.

In the steady state, if there is inflow of abyssal water into the basin, the integrated volume flux between the seabed and isopycnal γ ($\Psi(\gamma)$) increases monotonically approaching the upper boundary of the inflow, above which the flow reverses, and so must $G(\gamma)$. In other words, the net water mass transformation through the sequence of isopycnals increases as water becomes lighter. This increase must be associated with a concomitant increase in at least one of the terms of the decomposition in equation 6. We will argue below that the terms growing the fastest with decreasing γ are those proportional to $\partial S / \partial \gamma$, namely the terms g_F and g_q. This study, consistent with the global analysis of de Lavergne et al. (2016), shows that lighter abyssal waters tend to have larger bottom intercept areas, typically reaching a maximum for the density range corresponding to the upper boundary of abyssal waters.

4. Observations

4.1. Data Description

All observational data used in this study were collected between December 2014 and March 2015. The two cruises on RRS James Cook (JC112) and FS Sonne (SO238) were funded as part of the multi-institute research project OSCAR (Oceanographic and Seismic Characterization of heat dissipation and alteration by hydrothermal fluids at an Axial Ridge) that aims to investigate the coupling of hydrothermal flow between the ocean and the lithosphere and its impact on the evolution of the oceanic crust and on basin-scale circulation. All of the 132 conductivity-temperature-depth (CTD) casts went down to approximately 5 m above the bottom. The vertical distributions of temperature, salinity, and dissolved oxygen were measured with a SBE911plus CTD system (Sea-Bird Electronics, Inc.). The accuracy of the sensors was 0.001 °C, 0.0003 S/m, 1 dB, and 0.1 ml/l (4.47μmol/kg) for temperature, conductivity, pressure, and oxygen, respectively. This results in density accuracy of 0.004 kg/m^3. However, the precision of CTD sensors is much greater than their accuracy, which allows us to accurately evaluate density gradients as small as 10^{-5} kg/m^4 when defining the upper boundary of the wsBBL. The use of density gradient criteria to identify the wsBBL is discussed further in Banyte, Morales Maqueda, et al. (2018).

The geothermal heat flux in the basin was estimated by using the age map of the ocean floor (Müller et al., 1997) as a proxy for the heat flow. This sea floor age data set has a resolution of 0.1° × 0.1°. Then, we applied the formula of Stein and Stein (1992) linking the age of the bedrock to the heat flow through the crust: $q(t) = 510t^{-0.5}$, where t is crust age in million years (Myr) and q is the heat flow in milliWatt per square meter (mW/m^2). The ridges traversing the western side of the Basin stand out due to their large heat flow estimate (Figure 1). It is expected that the Stein and Stein (1992) formula overestimates the geothermal heat flux for very young crust, as their estimate in that case approaches infinity. Hence, we imposed an upper limit of 550 mW/m^2
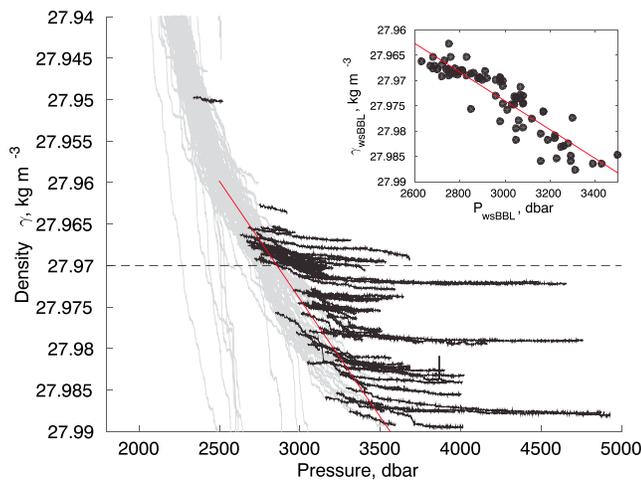
Figure 3. Vertical neutral density profiles (gray) with the wsBBL, identified by the search algorithm presented in Appendix A, marked in black. The horizontal dashed line marks the upper boundary of abyssal waters. The top right figure shows the density-pressure relation estimated at the top of wsBBL with their linear fit marked by the red line. wsBBL = weakly stratified bottom boundary layer.

on the geothermal heating estimates. The resulting difference in the total heat flux for the incrop of the $\gamma = 27.970 \pm 0.001$ kg/m^3 layer is estimated to be ~4%.

4.2. The Weakly Stratified Bottom Boundary Layer

To define the boundaries of the bottom intercept areas of density layers, the bottom densities of abyssal waters must be mapped. However, a near bottom density measurement might not represent abyssal waters if taken over shallow locations. Instead, the hydrographic data indicate that a thick wsBBL covers most of the basin (Figure 3). Assuming that thick wsBBL can only form at the bottom of the basin, but not over basin walls, such as shallow ridges, only profiles having a thick wsBBL were taken to map the bottom density.

The wsBBL was defined as the abyssal region where density gradients are smaller than 1×10^{-5} kg/m^4 (see details in Appendix A), computed over 50 m depth intervals. For this reason only stations with the estimated wsBBL thickness larger than 50 m were used for mapping. Of the 132 neutral density profiles in the Panama Basin, 78 had wsBBLs thicker than 50 m and, for these profiles, the median thickness of the wsBBL is 350 m; at seven sites the wsBBL was found to be over 1,000 m thick.

The density and pressure, γ_{wsBBL} and P_{wsBBL}, at the upper boundary of the weakly stratified bottom waters are highly correlated with one another (top right panel of Figure 3) and vary smoothly in space. This is a common property of abyssal waters observed over most of the global ocean basins (Banyte, Morales Maqueda, et al., 2018). Consequently, we use γ_{wsBBL} to map bottom density and the linear relation between γ_{wsBBL} and P_{wsBBL} to outline shallow bathymetry (Figure 4) with details given in Appendix B.

Taking the bathymetry into account, the density map reveals the pathway of abyssal waters as they fill the basin. The densest waters, as expected, are channeled along the deepest trenches in the eastern part of the basin. However, as they fill the basin, the bottom waters become lighter, and their P_{wsBBL} becomes shallower, which leads to weaker topographic constraints. In the east of the basin, the narrow trenches are the main arteries along which the dense water spreads. In the west, the similarly narrow trenches are completely flooded with nearly homogeneous bottom waters, the upper boundary of which is located some 800 m higher up in the water column (Figure 3). Overall, shallow P_{wsBBL} supports wsBBLs that can become over 1,000 m thick over deep trenches.

4.3. Incrops

The term incrop was used by de Lavergne et al. (2016) to refer to the bottom intercept area of ocean density layers, by analogy with the density layer outcrops at the sea surface. In the same way as outcrops at the sea surface can be associated with mixed layers hundreds of meters deep, incrops can result in equally thick wsBBLs along the abyssal water spreading path. However, nearly flat isopycnals can be interrupted by sloping
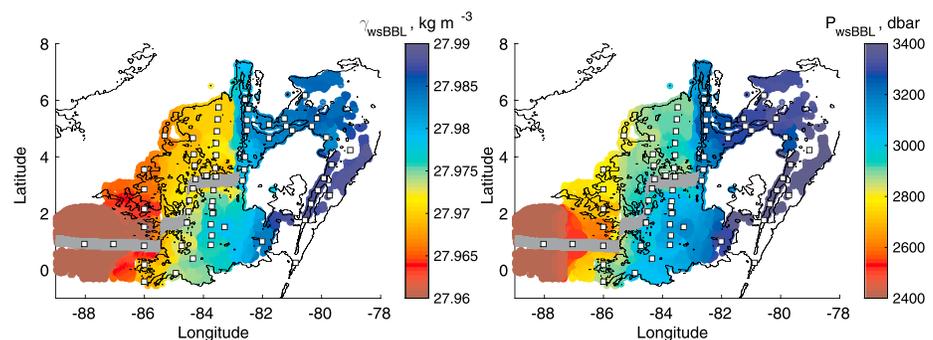
Figure 4. Map of interpolated γ_{wsBBL} (left) and recomputed P_{wsBBL} (right). The squares indicate the location of the conductivity-temperature-depth casts. The thin black line delineates the 2,900 m isobath, which approximately corresponds to the $P_{wsBBL}(\gamma = 27.970)$ value. The thick gray line indicates the location of the spreading axial ridges in the basin. wsBBL = weakly stratified bottom boundary layer.
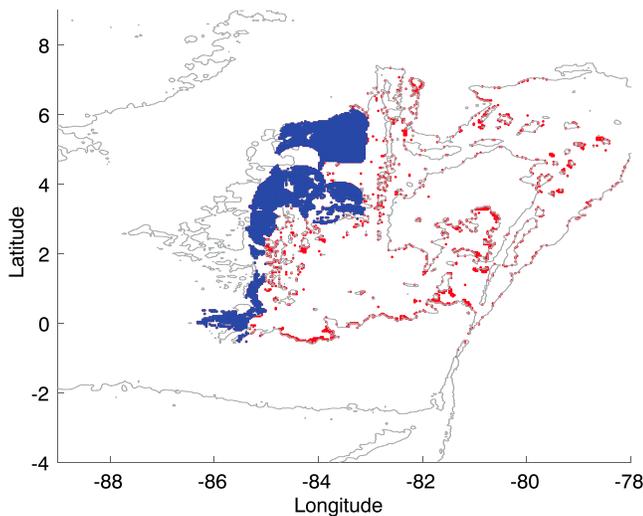
Figure 5. Spatial distribution of the largest bottom intercept area, corresponding to the neutral density layer $\gamma = 27.970 \pm 0.001$ kg/m^3. Blue dots mark the incrop area ΔS_I, while the red dots mark the bottom intercept at the walls of the basin computed as a residual of $\Delta S - \Delta S_I$. Black lines show the 3,000 m isobath.

bathymetry along continental slopes, oceanic ridges, and sea mounts, creating thin wsBBLs just a few meters thick, as observed for example on the continental slopes (e.g., Moum et al., 2004). We call the latter regions the walls of the basin.

In this study, only profiles with wsBBL thicker than 50 m were used for bottom density interpolation, as when the wsBBL is thin a CTD profile may not sample the densest water. The resulting bottom density map reflects the map of incrops—bottom intercept areas of discretized density layers that are allowed to have thick wsBBL if only bathymetry permitted it. At the same time, the bottom intercept areas at the sloping walls of the basin cannot be directly observed either from our data or from historical data sets, because most of the CTD profiles stop at least 5 m above the bottom. Instead, such areas are inferred from maps of stratification and bathymetry by assuming flat γ_{wsBBL} surfaces at the depth of P_{wsBBL}. In this way, the map of incrops as shown in Figure 4 can be complemented with the bottom intercept areas at the basin walls as shown in Figure 5 (details in Appendix B).

In the Panama Basin, the density layer $\gamma = 27.970 \pm 0.001$ kg/m^3 is estimated to have the largest incrop area: about 75% of the total bottom intercept area is estimated to reside over the western side of the basin, where this density layer intercepts the bottom of the basin, while the remaining 25% of the bottom intercept is located away from the incrop, along the continental slopes and the flanks of shallow ridges (Figure 5). However, while isopycnal $\gamma_{27.970}$ has the largest incrop area, the lighter isopycnal $\gamma_{27.950}$ finishes to fill the bottom of the basin. This means that all of the density layers lighter than $\gamma_{27.950}$ do not form incrops with thick wsBBL, but have bottom intercept areas at the walls of the basin forming very thin wsBBLs (less than 50 m thick). In this study, waters with densities higher than $\gamma = 27.970$ kg/m^3 are referred to as the abyssal water layer.

For abyssal waters, incrop areas tend to be larger for lighter densities (Figure 6c), reaching a maximum for the upper boundary of abyssal waters at $\gamma_{27.970}$. The bottom intercept areas at the basin walls are also slightly increasing with lighter waters, but less sharply than incrops. Furthermore, for most of the lighter abyssal waters, the areas of the bottom intercepts at the walls are smaller than the incrop areas for the same density layers. Therefore, although the total area of density layers is monotonically increasing as waters become lighter (Figure 6a), this does not mean that hypsometry (increase in the area of the ocean basins at shallower depths) defines the size of the bottom intercept areas for the abyssal waters in the basin.

The spatial extent of abyssal isopycnals is strongly controlled by transformation processes which prevent them from spreading uniformly through the basin (Figure 4). It is instructive to estimate the hypothetical intercept area of the abyssal waters in the basin if they could spread horizontally without transformation to fill the basin. In this case, the intercept area would be controlled purely by the basin average stratification and by hypsometry. We have done this calculation using the $P_{wsBBL} - \gamma_{wsBBL}$ relation discussed above (Figure 7). Bathymetry by itself would allow larger spatial extents of all abyssal waters up to the isopycnal $\gamma_{27.950}$, with the largest differences estimated below $\gamma_{27.970}$ isopycnal. Hence, the area of abyssal waters is controlled not by hypsometry but by the existence and extent of incrops.

4.4. Geothermal Heating Contribution to Water Mass Transformation

In a semienclosed basin, such as the Panama Basin, in steady state, volume conservation dictates that integrated abyssal water volume influx into the basin $\Psi(\gamma)$ is equal to water mass transformation across the abyssal water boundary γ. Hence, the isopycnal corresponding to the lightest abyssal waters that inflow into the Panama Basin through the Ecuador Trench passage will experience the largest diapycnal upwelling. They also happen to have the largest incrop area, as was shown above. Both turbulent diffusion and geothermal heating contribute to density flux divergence over the incrops (the terms g_F and g_q in equation (6) are always positive). In this section, we evaluate the contribution of geothermal heating to abyssal water mass transformation.

Geothermal heating in the Panama Basin is highly variable in space. The three spreading ridges on the western side of the basin emit large geothermal heat fluxes (Figure 1) in comparison to the basin average flux of 210 mW/m^2. Yet while heat fluxes directly over the ridges have in all likelihood an important effect on the local
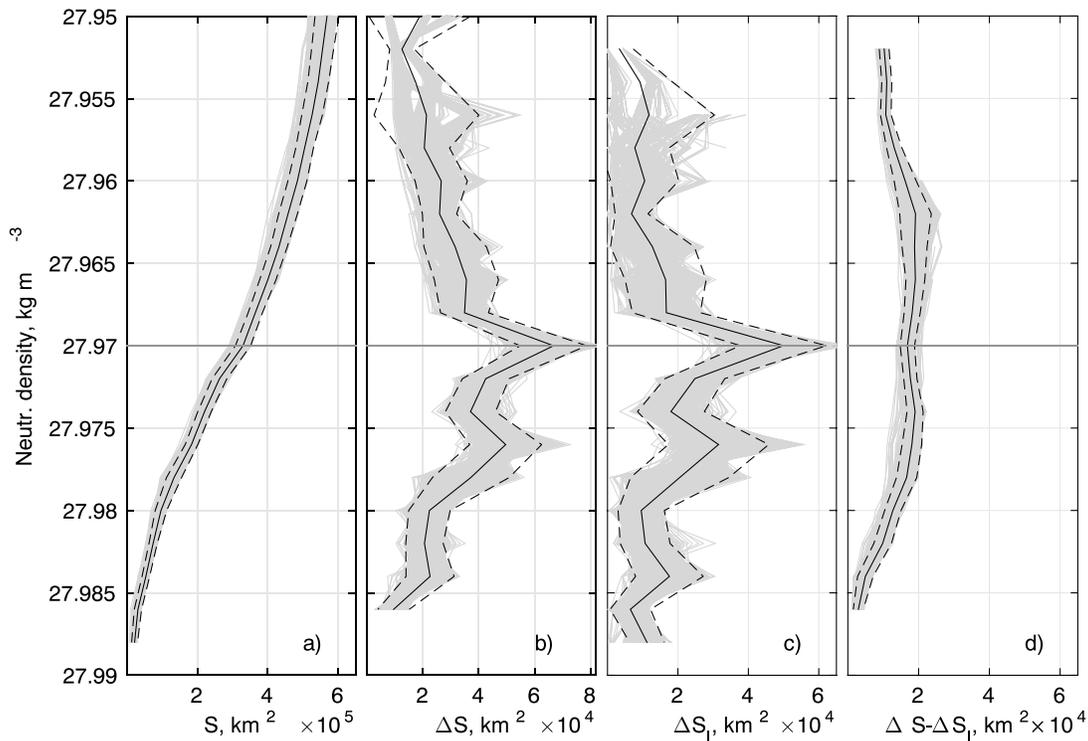
Figure 6. Surface area of the neutral density surfaces (a), bottom intercept area (b), incrop area (c), and bottom intercept area at the walls of the basin (d) computed as a residual of (b) − (c). Profiles in (b) to (d) are calculated for a density increment of 0.002 kg/m³. Gray lines represent the results of the spatial interpolation of randomly chosen 70% of the observed profiles repeated 1,000 times, their mean (solid black line) and two standard deviations (dashed line). The horizontal line marks the upper boundary of abyssal waters.

Figure 7. Ratio of the maximal area of a density layer allowed by hypsometry to the observed area: $S_{max}(\gamma)/S(\gamma)$.

circulation, the incrop areas of the lightest abyssal waters extend well beyond the ridges, which suggests that the contribution of geothermal hot spots to the total density flux divergence over the incrops is modest. For example, approximately 2% of the total bottom intercept area of the isopycnal 27.970 ± 0.001 kg/m³ is located above geothermal sources larger than 550 mW/m², contributing only 10% to the total water mass transformation associated with geothermal heating in this layer.

As spreading ridges are located on the western side of the basin, the average geothermal heating q enveloped by lighter densities is increasing, $\partial q/\partial \gamma < 0$ (Figure 8). Accordingly, the term g_{dq} in equation (6) is positive. For abyssal waters, the estimated average density gradient of q is of the order of -5 W·m⁻¹·kg⁻¹. Due to large incrop areas, abyssal waters have exceptionally small ratios of isopycnal surface area, S, to bottom intercept area, ΔS, which we show in the section below to be ~ 5 for density layers with $\Delta\gamma = 0.002$ kg/m³ increments. As a result, a comparison of terms g_{dq} and g_q reveals that g_{dq} is $\sim 25\%$ of g_q and has a nonnegligible contribution to the abyssal water upwelling.

The lightest abyssal water layer 27.970 ± 0.001 kg/m³ has the largest bottom intercept area and receives the largest amount of geothermal heat at around $(1.7 \pm 0.3) \times 10^{10}$ W (Figure 8); the error analysis for this estimate is presented in Appendix B. This geothermal heating is associated with an estimated abyssal water upwelling of $g_q = 0.32 \pm 0.07$ Sv across the density surface $\gamma_{27.970}$. These calculations have been made with a thermal expansion coefficient of $\alpha = (1.5 \pm 0.15) \times 10^{-4}$ per K and a heat capacity of seawater of $C_p = 3992$ J·kg⁻¹·K⁻¹. Since the abyssal water inflow into the basin is 0.29 ± 0.07 Sv (Banyte, Smeed, et al., 2018), these estimates show
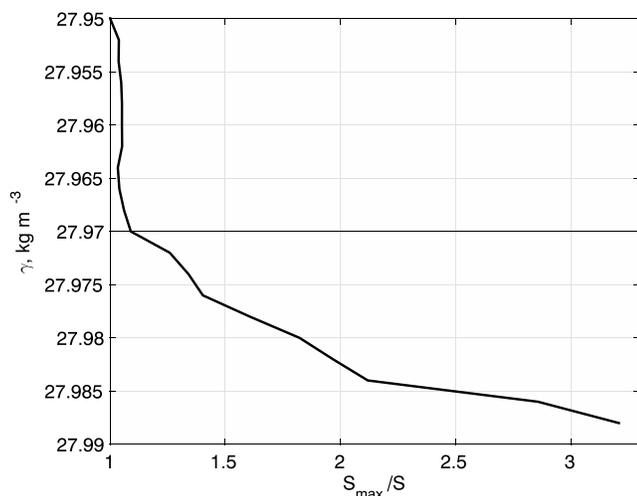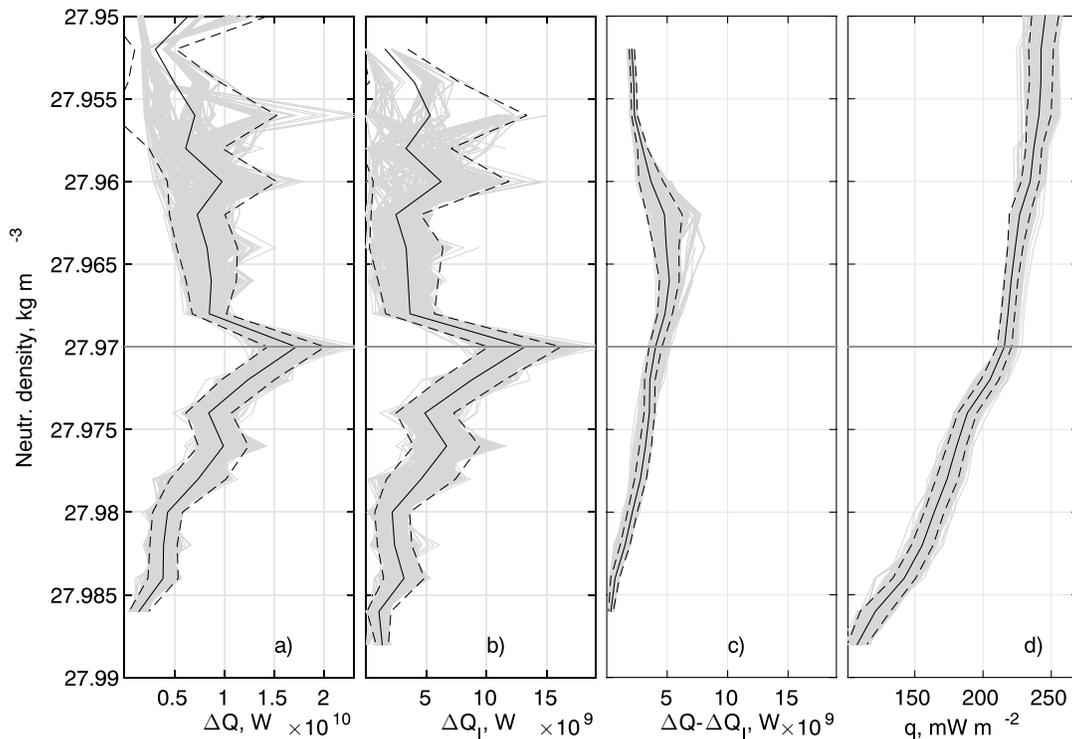
Figure 8. Geothermal heat fluxes over: (a) the total bottom intercept area of an isopycnal layer, (b) incrop area only, (c) basin wall, computed as a residual of (a) − (b), only. All profiles were calculated for a density increment of 0.002 kg/m³. The average geothermal heat flux over the entire area covered by an isopycnal is shown in (d). Gray lines represent the results of the spatial interpolation of randomly chosen 70% of the observed profiles repeated 1,000 times, their mean (solid black line) and two standard deviations (dashed line). The horizontal line marks the upper boundary of abyssal waters.

that geothermal heating is the dominant process causing water mass transformation in the basin, when away from the highly turbulent region of the Ecuador trench.

In conclusion, the abyssal water upwelling in the Panama Basin is strong both due to the strong geothermal heating, which is estimated to be three times the global average, and also due to the spatial distribution of geothermal hot spots located at the far-end from the abyssal water inflow passage.

### 4.5. The Influence of Stratification on Water Mass Transformation

Observations show that turbulent energy dissipation can increase by at least an order of magnitude over areas of rough topography (e.g., Waterhouse et al., 2014). The bottom intensification of mixing is only modest over smooth sea floors. Away from the boundaries, the ocean seems to have a more or less uniform background diffusivity of $K_b^z = 10^{-5}$ m²/s. This raises the question of how this small background diffusivity affects the abyssal and deep water upwelling in the Panama Basin. Here we investigate whether interior water upwelling driven by constant turbulent diffusivity in an environment where stratification increases rapidly above the wsBBL can be significant in comparison to water upwelling at the boundaries.

The total surface area of density layers (S) is significantly larger than the size of their bottom intercept areas (ΔS), especially for waters lying above the abyssal water layer. Stratification increases with height above the bottom, which with a large surface area of isopycnals, could dominate the vertical divergence of the turbulent density flux and, correspondingly, the diabatic upwelling in the basin's interior. For the case of weak background diffusivity, taken as a constant for both basin's interior and at the upper boundary of the wsBBL, the terms g_{dF} and g_F in equation (6) can be compared. In this case, density fluxes are parametrized as $F(\gamma) = K_b^z \gamma_z$.

Comparing terms g_{dF} and g_F in equation (6) with parametrized density fluxes

$$\frac{g_{dF}}{g_F} = \frac{\Delta\gamma_z S(\gamma)}{\gamma_z \Delta S(\gamma)}, \tag{7}$$

where the density discretization interval is $\Delta\gamma = 0.002$ kg/m³, $\Delta\gamma_z$ and $\Delta S(\gamma)$ are equal to $(\partial\gamma_z/\partial\gamma)\Delta\gamma$ and $(\partial S/\partial\gamma)\Delta\gamma$, respectively.
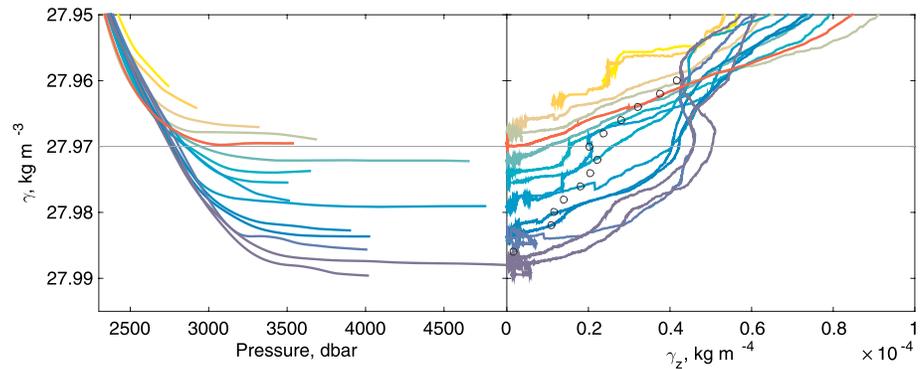
Figure 9. Average density-pressure (left) and density gradient profiles (right) over the incrops discretized with density increments of 0.002 kg/m³. The spatial average of γ_z along isopycnal weighted by the incrop areas is marked by empty circles. The red profile represents the average profile located over the largest incrop area of $\gamma_{27.970}$. The horizontal line marks the upper boundary of abyssal waters.

In general, the vertical density gradient is highly variable along any density surface: the strongest abyssal stratification occurs near the inflow passage of the Ecuador Trench and the weakest at the incrops. The incrops are, by definition, accompanied by thick wsBBLs. Above the wsBBL, the vertical isopycnal density gradient tends to increase with decreasing densities (right panel of Figure 9). However, the profiles near the Ecuador Trench demonstrate how ocean dynamics affect the abyssal water stratification: waters just above $\gamma_{27.970}$ have weaker density gradients than below. This is because these lighter waters are part of the outflow of homogenized deep waters from the Panama Basin into the open Pacific.

Despite the tendency for the stratification in any single water column to increase with decreasing density, the basin averaged stratification does not necessarily follow this pattern. The reason for this is the incrop area, and therefore the area of weak stratification, that gradually increases for lighter abyssal waters. Large incrop areas result in a large weight of weak stratification in the basin average of $\gamma_z(\gamma)$. In the Panama Basin, the basin average of $\gamma_z(\gamma)$ varies by less than 10% at the upper boundary of abyssal water layer, in the density range between $\gamma_{27.976}$ and $\gamma_{27.970}$ (black circles in right panel of Figure 9). Furthermore, the ratio of the total isopycnal surface area (S) to the bottom intercept area (ΔS) is also exceptionally small: varying between 2 and 7 (Figure 10), due to either large ΔS, or S being much smaller than hypsometry allows it: $S < S_{max}$ (Figure 7). As a result, diabatic abyssal water upwelling at the incrops dominates over the basin-wide abyssal water upwelling ($g_{dF}/g_F < 1$).
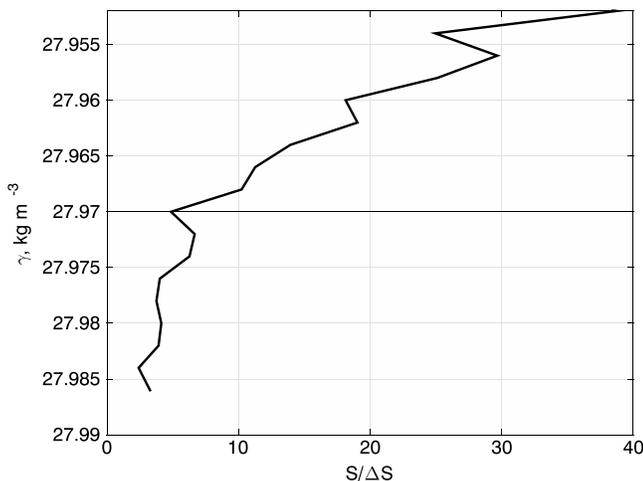
Figure 10. Ratio of the area of the isopycnal layer centered at γ to the bottom intercept area of the same layer: $S(\gamma)/\Delta S(\gamma)$, where $\Delta S(\gamma) = \frac{\partial S(\gamma)}{\partial \gamma}\Delta\gamma$ with $\Delta\gamma = 0.002$ kg/m³. The horizontal line marks the upper boundary of abyssal waters.

A reverse outcome is expected for the deep waters above the abyssal water layer. The ratio S to ΔS is expected to grow significantly for deep waters controlled by hypsometry. For example, for deep waters immediately above the abyssal water layer, the $S/\Delta S$ ratio grows rapidly from an estimated value of 5 for the density layer 27.970 ± 0.001 kg/m³, to 40 for the isopycnal $\gamma_{27.95}$ (at ~2,30 m depth), which is still within the semienclosed basin. At the same time, the basin average density gradient grows at the rate of 5×10^{-6} kg/m⁴ per density step of 0.002 kg/m³, reaching a density gradient of 8×10^{-5} kg/m⁴ for the same isopycnal of $\gamma_{27.95}$ (Figure 9), resulting in the ratio of 2.5 in equation (7). The ratio is expected to increase even further with lighter waters, following the increase of ratio $S/\Delta S$. As a result, upwelling of deep (but not abyssal) waters is much more likely to be basin-wide, along the whole density surfaces, as originally suggested by Stommel (1958), unless the bottom-intensified turbulence drives significant water mass transformation at the walls of the basin.

In conclusion, for abyssal waters, boundary upwelling is much more important than for the deep waters above them, because abyssal waters have access to the bottom of the basin resulting in formation of incrops
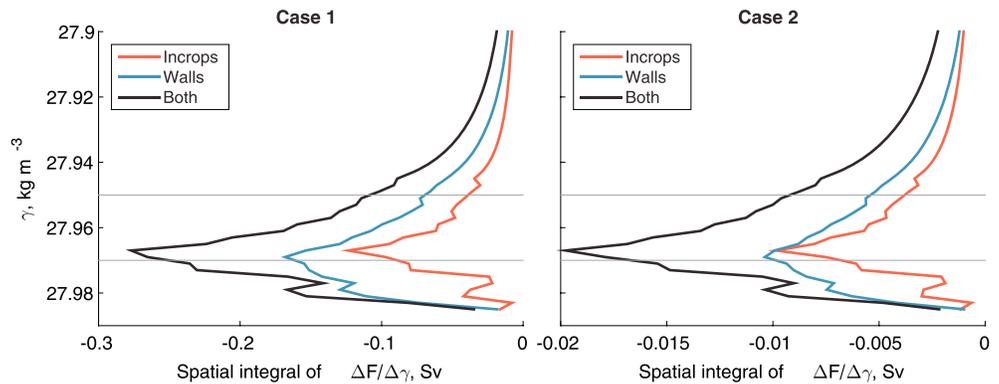
Figure 11. Spatial integral of density flux divergence above the weakly stratified bottom boundary layer for the exceptionally intense bottom intensification of turbulence (*Case 1*) and for the strong bottom intensification of turbulence (*Case 2*). The integration area is divided into sections: incrops, walls of the basin, where weakly stratified bottom boundary layer is very thin, and sum of both. Horizontal lines mark the upper boundary of the abyssal water layer $\gamma_{27.970}$ and the lightest isopycnal with the access to the bottom of the basin $\gamma_{27.95}$. Note the different *x* axis in two figures.

and, overall, exceptionally large bottom intercept areas of density layers. This becomes even more significant when turbulence intensifies with depth, which is investigated below.

4.6. Bottom-Intensified Mixing

To understand the turbulence-driven deep water mass transformation in the basin, a more realistic parametrization of turbulence must be implemented. Two scenarios are addressed here: (1) turbulent density flux is strong near the bottom and rapidly decreases with height above the bottom, and (2) turbulent density flux is an order of magnitude weaker near the bottom and only slowly decreases in height. The first case represents highly turbulent regions, while the second case corresponds to *normal* conditions.

Specifically, density flux is parametrized as an exponential function following Ferrari et al. (2016), with the reference to the global estimates of turbulent dissipation (ϵ) over ridges and rough topography (Waterhouse et al., 2014):

$$F(h) = F_0 e^{-h/d}, \tag{8}$$

where F_0 is density flux at the bottom, h is height above the bottom, and d is an e-folding scale of the exponential function. However, density fluxes only above the wsBBL were considered $h > P_{wsBBL}$, because wsBBL is a layer where mixing efficiency reduces due to a very weak stratification and diffusive density fluxes at the bottom are zero.

Following Ferrari et al. (2016), in *Case 1*, the case of extreme bottom intensification of turbulence, density fluxes are parametrized with parameters $F_0 = 2 \times 10^{-8}$ kg·m^{-2}·s^{-1}, and $d = 500$ m. Such a parametrization is comparable to the turbulent dissipation intensification measured over some parts of the mid-ocean ridges, where dissipation changes by an order of magnitude in 1,000 m above bottom (Waterhouse et al., 2014). In the case of normal turbulence enhancement with depth (*Case 2*), density fluxes are parametrized with parameters $F_0 = 2 \times 10^{-9}$ kg·m^{-2}·s^{-1}, and $d = 1,000$ m. Such parametrization is comparable to the turbulent dissipation intensification as measured over the rough topography (Waterhouse et al., 2014).

With turbulence increasing exponentially with depth, the largest turbulent density fluxes are found at the top of the wsBBL. Just above the P_{wsBBL}, the density flux convergence $\Delta F(\gamma)/\Delta \gamma$ is also at its maximum. Locally, both the density flux and its convergence decrease with lighter densities above the P_{wsBBL}. Furthermore, large incrop areas found for lightest abyssal waters result in large spatial integral of density flux convergence $< \Delta F(\gamma)/\Delta \gamma > S$ (details in Appendix D), which reaches a maximum just above the $\gamma_{27.970}$ surface (Figure 11).

The water mass transformation framework used in this study is formulated in density space, hence, density fluxes expressed against the height above the bottom must be converted to density units by using the local stratification profile. Stratification profiles as a function of density (see Figure 9) are averaged on density surfaces. Thus, having a map of the bottom density, local stratification may be estimated everywhere in the basin as well. Near the Ecuador Trench, the abyssal water source, abyssal and deep water stratifications, is the strongest, while over incrops it is the weakest. Hence, by using density flux parametrization as in equation (8),
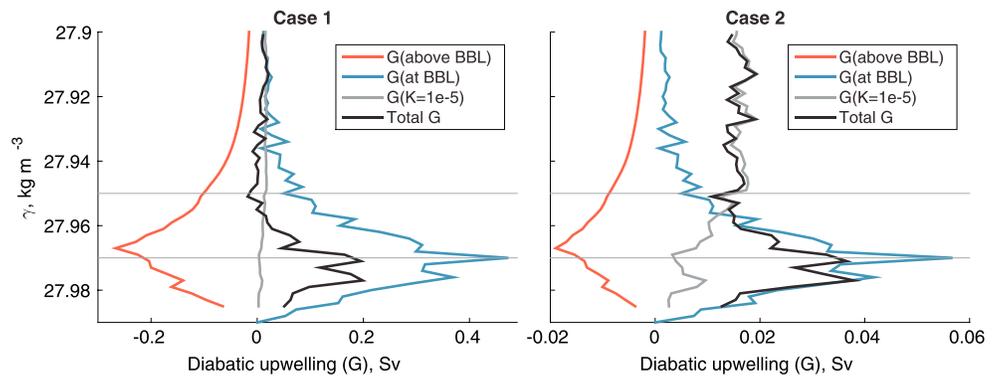
Figure 12. Spatially integrated density flux divergence in the Panama Basin for the exceptionally intense bottom intensification of turbulence (*Case 1*) and for the strong bottom intensification of turbulence (*Case 2*). The profiles show downwelling above weakly stratified BBL (red) and upwelling at the weakly stratified BBL (blue) driven by the bottom-intensified turbulence, the upwelling driven by the background turbulence (gray) and their total upwelling (black). Horizontal lines mark the upper boundary of the abyssal water layer and the lightest isopycnal with the access to the bottom of the basin. Note the different *x* axis in two figures. BBL = bottom boundary layer.

the bottom-intensified turbulence is much more compressed in density space at the western side of the basin, where the largest incrops are located. Finally, having the largest incrop area and weak stratification over it, the spatially integrated density flux divergence peaks sharply at $\gamma_{27.970}$ (Figure 11).

Nevertheless, despite the fact that the area of incrop is almost three times larger for $\gamma = 27.970 \pm 0.001$ than the bottom intercept area over the walls, the spatially averaged turbulent density flux convergence is similar over both the basin walls and the incrop. The reason is the extremely thin wsBBL found at the basin walls, where much larger turbulent density fluxes result at the upper boundary of the wsBBL. Due to variations in thickness of the wsBBL over incrops, the maximum density flux $F(\gamma)$ at the top of the wsBBL is on average twice as small as the chosen F_0 value (not shown).

Density flux convergence drives water downwelling. The area integral of this downwelling increases for lighter abyssal waters, reaches a maximum just above the abyssal water layer, and reduces with decreasing density for the deep waters above (Figure 12). The strength of the downwelling is highly sensitive to the chosen parametrization of density fluxes. With exceptionally strong bottom-intensified turbulence (Case 1), the largest downwelling amounts to 0.27 Sv, while upwelling at the wsBBL amounts to 0.47 Sv, which yields a total upwelling at the upper boundary of abyssal waters of ~0.2 Sv. An order of magnitude smaller $F(\gamma)$ yields an order of magnitude smaller water mass transformation rate with the total upwelling estimate of ~0.04 Sv.

Furthermore, it is interesting to observe that in the Case 2, the diabatic upwelling driven by the background turbulence of constant $K_b^z = 10^{-5}$ m²/s is relatively small for abyssal waters, but as soon as density layers stop having access to the bottom of the basin, above isopycnal $\gamma_{27.950}$, the background turbulence becomes dominant. However, we note that isopycnal $\gamma_{27.950}$ spreads at a depth of 2,300 m, and that waters above $\gamma_{27.950}$ become free to exchange with the tropical Pacific Basin through passages other than the Ecuador Trench. The incrops of those lighter waters are located outside the Panama Basin, and only a small part of their bottom intercepts are located at the walls of the Panama Basin.

In section 4.4, we have estimated that geothermal heating results in a diabatic upwelling rate across the upper boundary of abyssal water layer that has the same magnitude as the total inflow of abyssal waters into the basin of ~0.3 Sv. Hence, the turbulent simulation Case 2 with very weak contribution to the total diabatic upwelling of only ~0.04 Sv is a more reasonable scenario than Case 1. All the same, Case 2 represents a strong bottom intensification of turbulence that is comparable to the turbulent dissipation observed over rough topography (Waterhouse et al., 2014).

5. Summary and Discussion

The Panama Basin serves as a conveniently small observatory for abyssal water investigation. The basin is unique in having a single passage for abyssal water inflow into the basin, the magnitude of which is estimated to be 0.29 ± 0.07 Sv (Banyte, Smeed, et al., 2018) and a strong geothermal heating rate inside the basin. Banyte,

Smeed, et al. (2018) estimated that about half of the densest abyssal waters inflowing through the Ecuador Trench become lighter within a distance of 200 km downstream of the sill of the trench. This study analyses how abyssal waters upwell away from the intensely turbulent narrow passage.

Together with recent studies of Ferrari et al. (2016), and de Lavergne et al. (2016), McDougall and Ferrari (2017), we confirm that abyssal upwelling happens predominantly within the wsBBL, the latter being formed when isopycnals intercept the bottom of the basin, which we denote an incrop. The incrop areas increase as abyssal waters become lighter as they move from the eastern to the western side of the basin. Toward the west, geothermal heating also intensifies due to the presence of active spreading ridges. This study shows that abyssal water upwelling through its upper boundary ($\gamma_{27.970}$) is dominated by the geothermal heating integrated over the bottom intercept area of this water layer ($\gamma = 27.970 \pm 0.001$ kg/m^3).

Recent theories of abyssal water upwelling (de Lavergne et al., 2017; Ferrari et al., 2016; McDougall & Ferrari, 2017) are based on the assumption of a very thin (on the order of 10s of meters) bottom boundary layer, as are observed to occur in shallow waters (Moum et al., 2004). By contrast, in the Panama Basin, the wsBBL is hundreds to over a thousand meters thick at some places. Similarly, thick wsBBLs have been identified by Banyte, Morales Maqueda, et al. (2018) in the global ocean. We argue that oceanic basins have the bottom surfaces, which allow thick incrops to form. The thickness of the wsBBL can be used as a rule of thumb to functionally differentiate between the oceanic bottom and its walls.

Finally, we apply a common parametrization of the turbulence-driven density fluxes to evaluate the strength of the turbulence-driven upwelling at the wsBBL and of the downwelling above it. Due to the opposing effects of the exponential decrease of density fluxes with height above the bottom and a rapid rate of increase in the area of isopycnals, the maximum in the diabatic downwelling is found just above the upper boundary of the abyssal waters. Consequently, the strongest upwelling rate is estimated to occur in the lightest abyssal waters that have the largest incrop area. Nevertheless, the turbulence-driven upwelling that occurs within the wsBBL is always larger than the diabatic downwelling above the wsBBL.

In the Panama Basin, geothermal heating could account for almost all of the water mass transformation that is required to close the abyssal water layer mass balance. From this we deduce that turbulent dissipation is responsible for only a small part of the abyssal water mass transformation. This conclusion is confirmed by application of a commonly used parametrization of turbulent density fluxes over the rough topography (Case 2, in section 4.6), which predicts just 0.04 Sv of diapycnal upwelling.

Appendix A: Defining a Weakly Stratified Bottom Boundary Layer

The vertical density gradient γ_z was computed over each 50 m with a running step of 10 m. The wsBBL was defined where the vertical density gradient was smaller than 1×10^{-5} kg/m^4 and the thickness larger than 50 m. Sometimes, the water column of weak γ_z was interrupted by a short interval of high γ_z. In such cases, if the water column of weak γ_z was longer than the thickness of the interval with high γ_z, it was assumed that the latter was an intrusion and, thus, neglected.

Appendix B: Computing the Incrop Area

The γ_{wsBBL} was spatially interpolated with a nearest neighbor algorithm with 50 km radius. In case of no cast found, a 150-km radius was used, instead. Then, topography that was shallower than the parametrized P_{wsBBL} of the interpolated γ_{wsBBL} was removed. To evaluate how estimated incrop areas are affected by sampling, we ran 1,000 simulations with 70% of all the stations randomly sampled without repetition. The full area of the γ^i_{wsBBL} surface was estimated as the horizontal area of the abyssal region where densities are equal to or larger than γ^i_{wsBBL} and deeper than $P_{wsBBL}(\gamma_i)$.

The error of bottom intercept area estimates due to sparse sampling is by far the largest. It causes the error for the incrop area estimate of ~20% as shown by dashed lines in Figures 6 and 8. The error of linear fit between P_{wsBBL} and γ_{wsBBL}, by comparison, is much smaller and affects incrop estimates by ~5%. We could not assess the error caused by the geothermal heating parametrization, but assume it to be also much smaller than the sparse sampling error.

Appendix C: The Vertical Density Gradient

The individual vertical density profiles were grouped by their γ_{wsBBL} with discretization step of 0.002 kg/m^3. In the range of γ_{wsBBL} chosen from 27.900 to 27.990 kg/m^3, in total, 45 mean vertical density profiles representing an incrop area were found. Then, each averaged profile was smoothed with a low pass filter over 400-m intervals and interpolated on a grid with 1-m increments. The basin-wide average of γ_z along neutral density surface γ was computed as

$$< \gamma_z(\gamma) > = \frac{\sum_i \Delta S_l(\gamma_i)\gamma_z^i(\gamma)}{\sum_i \Delta S_l(\gamma_i)}, \tag{C1}$$

where summation is over a number of profiles, representative of the area of the discretized incrop (ΔS_l). The basin-wide average $< \gamma_z >$ for each density surface is marked by a black dot in Figure 9.

Appendix D: Bottom-Intensified Turbulent Density Fluxes

The turbulent density flux at the location i is computed by using the formula:

$$F^i(z) = F_0 e^{-\frac{H^i - z^i}{d}}, \tag{D1}$$

where H^i is a local seabed depth and z^i is the depth coordinate increasing with larger densities as in Figure 2. Only $z^i < P^i_{wsBBL}$ was considered.

The spatial integration of density fluxes over each discretized incrop is carried out by (1) converting $F^i(z)$ to density space ($F^i(\gamma)$), by using a mean stratification profile averaged over the incrop, (2) averaging $F^i(\gamma)$ spatially over the incrop area in density space with analogy to equation (3), and (3) multiplying by the size of an incrop area $\Delta S_l(\gamma)$:

$$\sum_{x(\gamma_i), y(\gamma_i)} < F(\gamma_i) > |_{incrop}\Delta S_l(\gamma_i). \tag{D2}$$

The spatial integration of density fluxes over bottom intercept areas of discretized density layers at the walls is carried out by (1) *coloring* the whole region on the walls, where *color* represents the discretized bottom density in the bottom density atlas, (2) converting $F^i(z)$ to density space ($F^i(\gamma)$) depending on the color of the location with corresponding stratification profile of the incrop, (3) averaging $F^i(\gamma)$ first over the *colored* regions, then over the whole bottom intercept area at the walls, and 4) multiplying by the size of the bottom intercept area at the walls $\Delta S - \Delta S_l(\gamma)$:

$$\sum_{x(\gamma_i), y(\gamma_i)} < F(\gamma_i) > |_{walls}(\Delta S(\gamma_i) - \Delta S_l(\gamma_i)). \tag{D3}$$

The density flux divergence is integrated in a similar way. For example, over incrops, the density flux divergence for isopycnal $\gamma_0 + \frac{d\gamma}{2}$ can be written as

$$\sum_{x(\gamma_i), y(\gamma_i)} (\frac{< F(\gamma_i + d\gamma) > - < F(\gamma_i) >}{\Delta \gamma})|_{incrop}\Delta S_l(\gamma_i). \tag{D4}$$

References

Adcroft, A., Scott, J. R., & Marotzke, J. (2001). Impact of geothermal heating on the global ocean circulation. *Geophysical Research Letters*, *28*, 1735–1738.

Banyte, D., Morales Maqueda, M., Hobbs, R. W., Smeed, D., Megann, A., & Recalde, S. (2018). Geothermal heating in the Panama Basin I: Hydrography of the basin, *Journal of Geophysical Research: Oceans*, *123*. https://doi.org/10.1029/2018JC013868

Banyte, D., Smeed, D., & Morales Maqueda, M. A. (2018). The weakly stratified bottom boundary layer of the global ocean. *Journal of Geophysical Research: Oceans*. https://doi.org/10.1029/2018JC013754

de Lavergne, C., Madec, G., le Sommer, J., Nurser, A. J. G., & Garabato, A. C. N. (2016). On the consumption of Antarctic Bottom Water in the abyssal ocean. *Journal of Physical Oceanography*, *46*, 635–661.

de Lavergne, C., Madec, G., Roquet, F., Holmes, R. M., & McDougall, T. J. (2017). Abyssal ocean overturning shaped by seafloor distribution. *Nature*, *551*, 181–186.

Emile-Geay, J., & Madec, G. (2009). Geothermal heating, diapycnal mixing and the abyssal circulation. *Ocean Science*, *5*, 203–217.

Ferrari, R., Mashayek, A., McDougall, T. J., Nikurashin, M., & Campin, J. M. (2016). Turning ocean mixing upside down. *Journal of Physical Oceanography*, *46*(11), 2674–2686. https://doi.org/10.1175/JPO-D-15-0244.1

Hofmann, M., & Morales Maqueda, M. A. (2009). Geothermal heat flux and its influence on the oceanic abyssal circulation and radiocarbon distribution. *Geophysical Research Letters*, *36*, L03603. https://doi.org/10.1029/2008GL036078

Jackett, D. R., & McDougall, T. J. (1997). A neutral density variable for the world's oceans. *Journal of Physical Oceanography*, *27*, 237–263.

Klocker, A., & McDougall, T. J. (2010). Influence of the nonlinear equation of state on global estimates of dianeutral advection and diffusion. *Journal of Physical Oceanography*, *40*, 1690–1709. https://doi.org/10.1175/2010JPO4303.1

Ledwell, J. R., Montgomery, E. T., Polzin, K. L., St. Laurent, L. C., Schmitt, R. W., & Toole, J. M. (2000). Evidence for enhanced mixing over rough topography in the abyssal ocean. *Nature*, *403*, 179–182.

McDougall, T. J., & Ferrari, R. (2017). Abyssal upwelling and downwelling driven by near-boundary mixing. *Journal of Physical Oceanography*, *47*, 261–283.

Moum, J. N., Perlin, A., Klymak, J. M., Levine, M. D., Boyd, T., & Kosro, P. M. (2004). Convectively driven mixing in the bottom boundary layer. *Journal of Physical Oceanography*, *34*, 2189–2202.

Müller, R. D., Roest, W. R., Royer, J. Y., Gahagan, L. M., & Sclater, J. G. (1997). Digital isochrons of the world's ocean floor. *Journal of Geophysical Research*, *102*, 3211–3214.

Munk, W. H. (1966). Abyssal recipes. *Deep Sea Research and Oceanographic Abstracts*, *13*, 707–730.

Nurser, A. J., Marsh, R., & Williams, R. G. (1999). Diagnosing water mass formation from air–sea fluxes and surface mixing. *Journal of Physical Oceanography*, *29*, 1468–1487.

Polzin, K. L., Toole, J. M., Ledwell, J. R., & Schmitt, R. W. (1997). Spatial variability of turbulent mixing in the abyssal ocean. *Science*, *276*, 93–96.

Stein, C. A., & Stein, S. (1992). A model for the global variation in oceanic depth and heat flow with lithospheric age. *Nature*, *359*, 123–129.

Stommel, H. (1958). The abyssal circulation. Letter to the editors. *Deep Sea Research*, *5*, 80–82.

Walin, G. (1982). On the relation between sea-surface heat flow and thermal circulation in the ocean. *Tellus*, *34*, 187–195.

Waterhouse, A. F., MacKinnon, J. A., Nash, J. D., Alford, M. H., Kunze, E., Simmons, H. L., et al. (2014). Global patterns of diapycnal mixing from measurements of the turbulent dissipation rate. *Journal of Physical Oceanography*, *44*, 1854–1872.